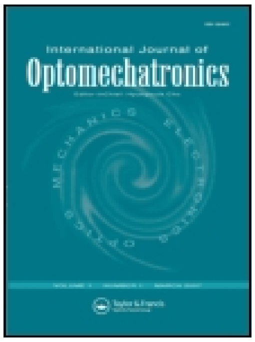

International Journal of Optomechatronics

ISSN: 1559-9612 (Print) 1559-9620 (Online) Journal homepage: https://www.tandfonline.com/loi/uopt20

Electromagnetic Steering of a Magnetic Cylindrical Microrobot Using Optical Feedback Closed-Loop Control

Ali Ghanbari , Pyung H. Chang , Bradley J. Nelson & Hongsoo Choi

International Journal of Optomechatronics, 8: 129–145, 2014

ISSN: 1559-9612 print/1559-9620 online
DOI: 10.1080/15599612.2014.901454

ELECTROMAGNETIC STEERING OF A MAGNETIC CYLINDRICAL MICROROBOT USING OPTICAL FEEDBACK CLOSED-LOOP CONTROL

Ali Ghanbari,[1] Pyung H. Chang,[1] Bradley J. Nelson,[1,2,3] and Hongsoo Choi[1,2]

[1]*Robotics Engineering Department, Daegu Gyeongbuk Institute of Science and Technology (DGIST), Daegu, South Korea*
[2]*DGIST-ETH Microrobot Research Center, DGIST, Daegu, Korea*
[3]*Institute of Robotics and Intelligent Systems, ETH Zurich, Zurich, Switzerland*

Control of small magnetic machines in viscous fluids may enable new medical applications of microrobots. Small-scale viscous environments lead to low Reynolds numbers, and although the flow is linear and steady, the magnetic actuation introduces a dynamic response that is nonlinear. We account for these nonlinearities, and the uncertainties in the dynamic and magnetic properties of the microrobot, by using time-delay estimation. The microrobot consists of a cylindrical magnet, 1 mm long and 500 μm in diameter, and is tracked using a visual feedback system. The microrobot was placed in silicone oil with a dynamic viscosity of 1 Pa.s, and followed step inputs with rise times of 0.45 s, 0.51 s, and 1.77 s, and overshoots of 37.5%, 33.3%, and 34.4% in the x, y, and z directions, respectively. In silicone oil with a viscosity of 3 Pa.s, the rise times were 1.04 s, 0.72 s, and 2.19 s, and the overshoots were 47.8%, 48.5%, and 86.8%. This demonstrates that closed-loop control of the magnetic microrobot was better in the less viscous fluid.

Keywords: closed-loop control, magnetic actuation, magnetic microrobot, time-delay estimation, visual feedback

1. INTRODUCTION

Micro- and nanorobots are expected to provide new biomedical applications in many fields, including localized therapies, diagnosis, targeted drug delivery, minimally invasive surgery, and cell transportation.[1,2] Sub-micron scale robots are preferred for *in-vivo* medical operations, as they can access small areas without traditional surgery, which may lead to shorter operation and recovery times. The environment in which the micro- and nanorobots will operate can be described as having a small Reynolds number (Re), where viscous forces are dominant over the inertial force. This low-Re environment has different fluid dynamics at the micro- and nanoscale compared with those at the macroscale.

Address correspondence to Hongsoo Choi, 50-1 Sang-Ri, Hyeonpung Myeon, Dalseong-Gun, Daegu, Republic of Korea. E-mail: mems@dgist.ac.kr

Color versions of one or more of the figures in the article can be found online at www.tandfonline.com/uopt.

NOMENCLATURE

B	magnetic flux density	**a**	acceleration
F	force	**e**	error
I	current	m	mass
K	gain	t	time
L	length	u	velocity
M	magnetization	δ	time delay
P	position	ζ	damping ratio
R	radius	η	dynamic viscosity
Re	Reynolds number	ρ	density
T	torque	ω	frequency

The dynamics of low-Re systems are steady and linear; however, magnetic actuation of microrobots introduces nonlinearities. Hence, for accurate closed-loop control the dynamic behavior of micro- and nanorobots should be explored further to overcome these nonlinearities. Such dynamic modeling is challenging at the micro- and nanoscale because the environment is extremely viscous, and because of the nonlinearities of magnetic actuation systems. In addition, the relationship between velocity and drag is known only for simple geometrical shapes, and approximations may be required for more complex shapes.

Magnetic objects typically sink in fluids, including water and silicone oil, due to the greater density of the magnetic material. Therefore, a three-dimensional position control system is needed to compensate for the weight of the microrobot.[3] However, fabrication and measurement errors introduce uncertainties into the weight and buoyancy force of a microrobot. The hydrodynamic drag force is another source of uncertainty in microrobot dynamics. The drag force exerted by a fluid on an object is linearly related to the velocity of the object in low Reynolds number flows ($\mathrm{Re} \ll 1$). The drag coefficient, which relates the drag force and velocity, varies for different microrobot shapes and orientations; it has been formulated only for special body shapes and can only be measured experimentally. However, it is difficult to make drag force measurements of objects with arbitrary shapes when the Re is small. Hence, the viscous drag forces on micro- and nanoscale objects and their weight introduce uncertainties into the dynamic model. The wall effects are also significant in the motion of micro- and nanoswimmers, and these effects are not well understood. In certain applications, there may be additional forces that are difficult to model, including contact, van der Waals, stiction, and electrostatic forces. The magnetic nonlinearities, inaccurate dynamic parameters, and uncertain forces make dynamic modeling and closed-loop control of swimming microrobots challenging.

To propel magnetic objects in a low-Re environment, bioinspired micro- and nanorobots can exploit artificial flagella and cilia.[4] These biomimetic robots generate propulsion by rotation of their helical flagella[5,6] or by forming planar waves via the flagella[7] or cilia.[8,9] Other magnetic microrobots may be directly manipulated by an external magnetic field gradient.[10,11] Mathieu et al.[10] used a magnetic resonance imaging (MRI) system to actuate magnetized particles and demonstrated that millimeter-sized ferromagnetic spheres can be propelled inside larger-diameter sections of arterial systems by using a field gradient of a few tens of mT/m, which is within the range of MRI systems. However, for smaller microrobots, larger magnetic field gradients are required. Yesin et al.[11] steered an elliptical micron-sized robot, with applications within different bodily fluids, by using Helmholtz and Maxwell coils that generated a magnetic field gradient of 0.7 T/m and a magnetic field strength of 0.2 T. The same group later developed a customized magnetic actuation system, which utilized superimposed magnetic fields from a number of electromagnetic coils to generate gradients of more than 2 T/m.[12,13] This system was used to propel microrobots by using an open-loop control system.

To enable automatic closed-loop motion control of magnetic agents, a position feedback system is required. One approach is to use the imaging capability of MRI systems.[14–16] The imaging modality of MRI systems is suitable for steering microrobots during endovascular procedures.[14] However, the positioning accuracy that is achievable using MRI is relatively poor.[15] The use of charge-coupled device (CCD) array cameras, along with microscopic lenses, is another approach to achieve optical feedback to determine the position of a microrobot.[17–19] This optical system has been proposed for assisting in eye surgery for minimally invasive intraocular operations.[19] In addition, Bergeles et al.[20] developed a model to localize a microrobot inside a human eye using a camera. The use of two or more high-speed cameras increases the number of degrees of freedom of the control system and can provide accurate real-time position feedback.

In this article, we report closed-loop control of the dynamics of a cylindrical magnetic microrobot. The model contains uncertainties as well as unknown dynamic parameters. We use a time delay estimation (TDE) controller to compensate for the uncertainties and unknown dynamics to control a cylindrical-type microrobot in three degrees of freedom (i.e., three-dimensional translational motion). TDE accounts for an estimate of the instantaneous values of the uncertain parameters in the input control forces based on the data from the previous iteration of the control process. An optical system provides feedback on the position of the microrobot. The TDE controller was designed based on a second-order error dynamics model and requires only minimal information of the system dynamics.

The remainder of this article is organized as follows. In Section 2 we derive the dynamic model and formulation for control of the microrobot. In Section 3, we describe the required physics for magnetic actuation in a low-Re environment. In Section 4, the experimental apparatus and results are described. Section 5 summarizes the article.

2. DYNAMIC MODELLING AND CONTROL

The aim of the model is to obtain control over the three-dimensional (3-D) translational motion of a magnetic cylinder (i.e., a microrobot) in a viscous fluid. Figure 1 shows a schematic diagram of the forces applied to the microrobot. The magnetic force, $\mathbf{F}_{\mathrm{m}}$, applied to propel the microrobot to overcome the forces owing to hydrodynamic drag, $\mathbf{F}_{\mathrm{h}}$, gravity, $\mathbf{F}_{\mathrm{g}}$, buoyancy, $\mathbf{F}_{\mathrm{b}}$, stiction, $\mathbf{F}_{\mathrm{s}}$, and drift, $\mathbf{F}_{\mathrm{d}}$, must balance with inertia as follows:

$$\mathbf{F}_{\mathrm{m}} + \mathbf{F}_{\mathrm{h}} + \mathbf{F}_{\mathrm{g}} + \mathbf{F}_{\mathrm{b}} + \mathbf{F}_{\mathrm{s}} + \mathbf{F}_{\mathrm{d}} = m\mathbf{a}, \tag{1}$$

where m is the mass and $\mathbf{a}$ is the acceleration of the microrobot.

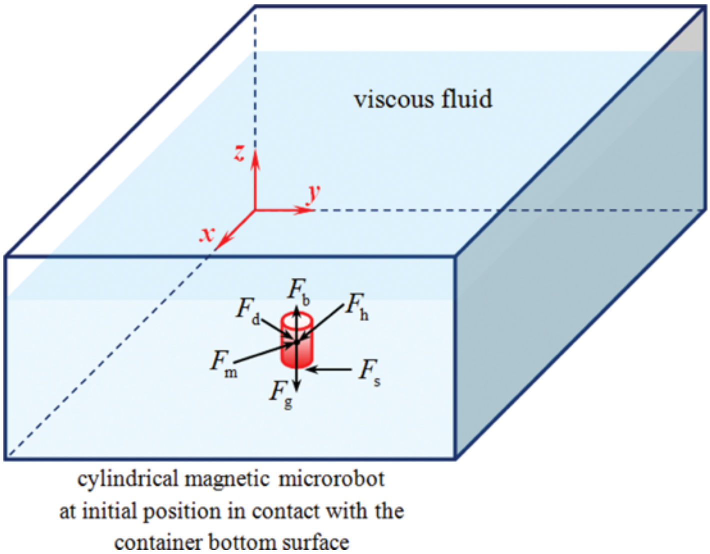

Figure 1. Schematic diagram showing the cylindrical microrobot moving in a viscous fluid and the coordinate system. The magnetic, $\mathbf{F}_{\mathrm{m}}$, hydrodynamic drag, $\mathbf{F}_{\mathrm{h}}$, gravity, $\mathbf{F}_{\mathrm{g}}$, buoyancy, $\mathbf{F}_{\mathrm{b}}$, stiction, $\mathbf{F}_{\mathrm{s}}$, and drift, $\mathbf{F}_{\mathrm{d}}$, forces on the microrobot are illustrated.

The dynamic system described by Equation (1) includes uncertain forces, i.e., gravity, drag, and buoyancy, as well as forces that are difficult to model, i.e., stiction and drift towards the walls. In the presence of these uncertainties and complex dynamics, a closed-loop control that uses model-based algorithms is challenging. We developed a controller that compensates for the uncertainties and complex dynamics through the implementation of TDE.[21–24]

To formulate the TDE controller, we rewrite Equation (1) with only the magnetic force on one side, and substitute the acceleration with the second time derivative of the position vector, i.e.,

$$\mathbf{F}_{\mathrm{m}} = m\ddot{\mathbf{P}} - (\mathbf{F}_{\mathrm{h}} + \mathbf{F}_{\mathrm{g}} + \mathbf{F}_{\mathrm{b}} + \mathbf{F}_{\mathrm{s}} + \mathbf{F}_{\mathrm{d}}). \tag{2}$$

Then, $\overline{m}\ddot{\mathbf{P}}$ is added to and subtracted, resulting in

$$\mathbf{F}_{\mathrm{m}} = \bar{m}\ddot{\mathbf{P}} + \mathbf{H}, \tag{3}$$

where $\overline{m}$ is a constant and $\mathbf{H} = (m - \overline{m})\ddot{\mathbf{P}} - \left(\mathbf{F}_{\mathrm{h}} + \mathbf{F}_{\mathrm{g}} + \mathbf{F}_{\mathrm{b}} + \mathbf{F}_{\mathrm{s}} + \mathbf{F}_{\mathrm{d}}\right)$ includes all of the uncertain terms. We construct the input control force, $\mathbf{F}_{\mathrm{m}}$, from

$$\mathbf{F}_{\mathrm{m}} = \bar{m}\mathbf{V} + \hat{\mathbf{H}}, \tag{4}$$

where $\hat{\mathbf{H}}$ is an estimate of $\mathbf{H}$, and $\mathbf{V}$ is given by

$$\mathbf{V} = \ddot{\mathbf{P}}_{\mathrm{d}} + K_v(\dot{\mathbf{P}}_{\mathrm{d}} - \dot{\mathbf{P}}) + K_p(\mathbf{P}_{\mathrm{d}} - \mathbf{P}), \tag{5}$$

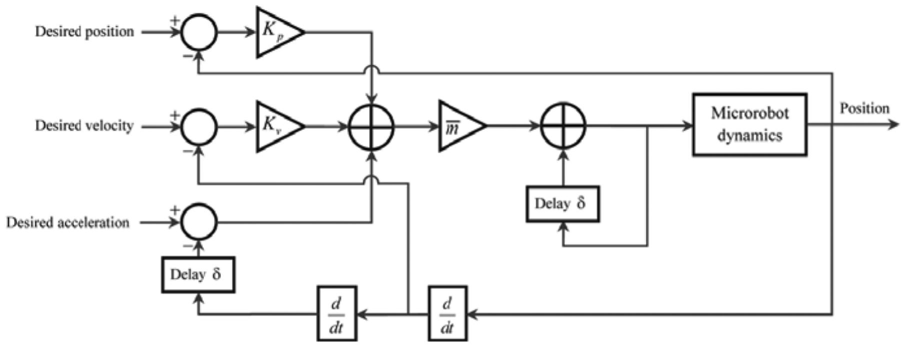

Figure 2. Schematic diagram illustrating the TDE controller with two design parameters, K_p and K_v, and one tuning parameter, $\overline{m}$.

where $\mathbf{P}_\mathrm{d}$ is the desired position vector, and K_p and K_v are the proportional and derivative gains, respectively. Assuming that $\hat{\mathbf{H}}$ is a sufficiently accurate estimate of $\mathbf{H}$, we can substitute Equations (4) and (5) into Equation (3), resulting in the following second-order differential equation describing the closed-loop error dynamics:

$$\ddot{\mathbf{e}} + K_v\dot{\mathbf{e}} + K_p\mathbf{e} \approx 0, \tag{6}$$

where $\mathbf{e} = \mathbf{P}_\mathrm{d} - \mathbf{P}$ is the position error. We design K_p and K_v so that the error dynamics exhibit the desired response.

Provided that the terms included in $\mathbf{H}$ are continuous or piecewise continuous, they can be estimated using the time-delayed values of the system variables from the previous iteration of the control system. Therefore, we use $\hat{\mathbf{H}}(t) = \mathbf{H}(t-\delta)$ to estimate $\mathbf{H}(t)$. We calculate $\mathbf{H}(t-\delta)$ using Equation (3) and substitute the result, along with Equation (5), into Equation (4), which leads to the following expression for the input force:

$$\mathbf{F}_\mathrm{m}(t) = \bar{m}(\ddot{\mathbf{P}}_\mathrm{d} + K_v\dot{\mathbf{e}} + K_p\mathbf{e}) + \mathbf{F}_m(t-\delta) - \bar{m}\ddot{\mathbf{P}}(t-\delta). \tag{7}$$

The parameter $\overline{m}$ is used to tune the performance of the controller. Figure 2 shows a schematic diagram describing the operation of the control system. Note that, to obtain Equation (7), we did not model the hydrodynamic, gravity, buoyancy, stiction, or drift forces. This simplifies the design of the controller and means that the control algorithm is not computationally expensive.

3. PHYSICS OF MAGNETIC ACTUATION AT LOW RE NUMBERS

3.1. Magnetic Actuation

Applying an external magnetic field to a cylinder that is magnetized along the longitudinal axis generates a magnetic torque, $\mathbf{T}_\mathrm{m}$, and aligns the cylinder to the magnetic field direction with a magnetic moment, $\mathbf{M}$, i.e.,

$$\mathbf{T}_\mathrm{m} = \mathbf{M} \times \mathbf{B}(\mathbf{P}), \tag{8}$$

where $\mathbf{B}$ is the magnetic flux density at position $\mathbf{P}$. Generating a spatial gradient in the magnetic field flux density will impose a propelling force on the microrobot. In such a non-uniform magnetic field, the magnetic force on a magnetized body with a magnetic moment $\mathbf{M}$ is given by

$$\mathbf{F}_{\mathrm{m}} = (\mathbf{M} \cdot \nabla)\mathbf{B}(\mathbf{P}). \tag{9}$$

Assuming ideal coils and a linear response of the magnetic cores, the magnetic field can be described by the linear superposition of the individual fields of several electromagnetic coils. The magnetic field of each coil is proportional to the current passing through the coil. Therefore, we can relate the magnetic torque and force to the set of currents in the coils, $\mathbf{I}$, using a coefficient matrix, $\mathbf{K}$, which is a function of the position and magnetic moment of the microrobot, i.e.,

$$\begin{bmatrix} \mathbf{T}_{\mathrm{m}} \\ \mathbf{F}_{\mathrm{m}} \end{bmatrix} = \mathbf{K}(\mathbf{P}, \mathbf{M})\mathbf{I}. \tag{10}$$

The coefficient matrix in Equation (10) is modeled and calibrated to map the field and gradient field at any point within a workspace.[12] Once the desired direction and input force are known, we may multiply both sides of Equation (10) by the pseudoinverse of the coefficient matrix evaluated at the position of the microrobot to find the required currents of the coils.

3.2. Hydrodynamic Drag Force

When the cylinder is aligned with the z-axis, the drag force can be obtained from Ref.[25] as shown in the following:

$$\mathbf{F}_{\mathrm{h}} = -\begin{bmatrix} \frac{4\pi\eta L}{\ln(7.4/Re)} & 0 & 0 \\ 0 & \frac{4\pi\eta L}{\ln(7.4/Re)} & 0 \\ 0 & 0 & 6\pi\eta R \end{bmatrix} \dot{\mathbf{P}}, \tag{11}$$

where R is the radius and L is the length of the cylinder, η is the viscosity of the fluid, and $\mathrm{Re} = 2\rho u R/\eta$ is the flow Re number, where u is the mean velocity and ρ is the density of the fluid. We approximate the drag force of the cylinder in the z direction by the drag of a sphere at low Re.

3.3. Stiction

The microrobot is in contact with the container surface at its first position, and there is high adhesion between the microrobot and the surface when it is pulled normally. The adhesion is inversely related to the size of the contact area, and is significant for microscale devices. At this scale, high static friction is also present between the microrobot and the surface during sliding. The term stiction refers to both adhesion due to van der Waals forces and friction forces. These forces are difficult to model,[26] but they introduce uncertainty in the dynamics of a microrobot with closed-loop control.

3.4. Drift

Viscous drag forces are larger when a microrobot moves near a solid boundary. Hydrodynamic interactions between the microrobot and the container walls produce a drifting effect that becomes more significant as the viscosity of the fluid increases. Lauga et al.[27] modeled bacteria swimming near a surface in a circular path due to the wall effect. However, since swimming methodologies differ between bacteria and a magnetically pulled microrobot, such a model cannot be applied to account for the drift of an artificial swimmer. However, the drift changes the trajectory of the microrobot, which requires compensation in the control law. The proposed TDE controller compensates for this effect by estimating the drift in the control system.

4. SIMULATION AND EXPERIMENT

We implemented the TDE controller using the experimental setup shown in Figure 3(*a*), which includes a magnetic actuation system, two cameras (GRAS-50S5C-C, Point Grey CCD Camera, Point Grey Research Inc., Vancouver, Canada), with lenses (VZM 600i, Edmund Optics Inc., Barrington, NJ, USA), camera holders, and a set of LEDs. The microrobot was placed in silicone oil inside a plastic cube that was located on top of the actuation system (Figure 3(*a*)).

We used a Minimag magnetic actuation system (Aeon Scientific, Zurich, Switzerland), which was composed of eight coils arranged in the configuration shown in Figure 3(*b*). The coils focus on a $10\,\text{mm} \times 10\,\text{mm} \times 10$-mm workspace, which is located 20 mm from the center of each coil.[12,13] By passing a current through each coil, a magnetic field is generated within the workspace.

The microrobot was a cylindrical NdFeB permanent magnet, 500 μm in diameter and 1000 μm in length. The density of the microrobot was $7450\,\text{kg/m}^3$, the mass was 1.46 mg, and the magnetic moment was $0.00027\ \text{A}{\cdot}\text{m}^2$. We used silicone oil with two different dynamic viscosities, i.e., 1 Pa·s and 3 Pa·s (KF96-1000CS and KF96-3000CS, Shin-Etsu Silicone Korea Co., Seoul, Korea). In the absence of a magnetic field, the microrobot sank in both fluids due to the higher density of the NdFeB compared with that of the silicone oil.

The position of the microrobot was determined using two cameras: one providing a top view and the other providing a side view, which was inclined at 17° relative to the horizontal plane. The microrobot was detected and tracked using background subtraction, and the position of the moving object was estimated after filtering out motion noise using morphological operations.[28] The tracking system rendered the images and was used to find the visible edges of the moving object. Then a rectangle was constructed based on the detected edges. The center of this rectangle coincided with the center of the microrobot, whose position was tracked. Hence for detection by the tracking system, the microrobot was first manipulated manually. When it was detected in two camera images, its position was used in the control system. The microrobot could be manually manipulated to the initial position, which was optionally located at the workspace origin. The cameras operated with a refresh rate of 15 Hz and a resolution of 1024×768 pixels, and with a frequency of 60 Hz at a resolution of 800×600 pixels. The sampling frequency of the cameras was the limiting factor for the overall sampling frequency of the system, as the other devices had higher sampling rates (for instance, the data-acquisition cards had a

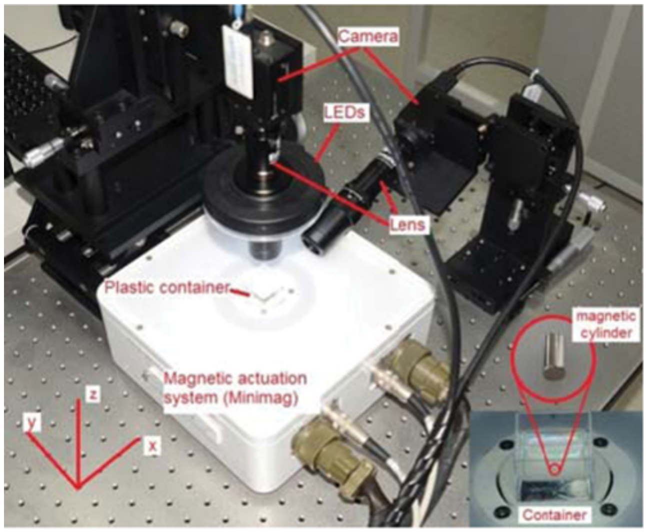

(*a*)

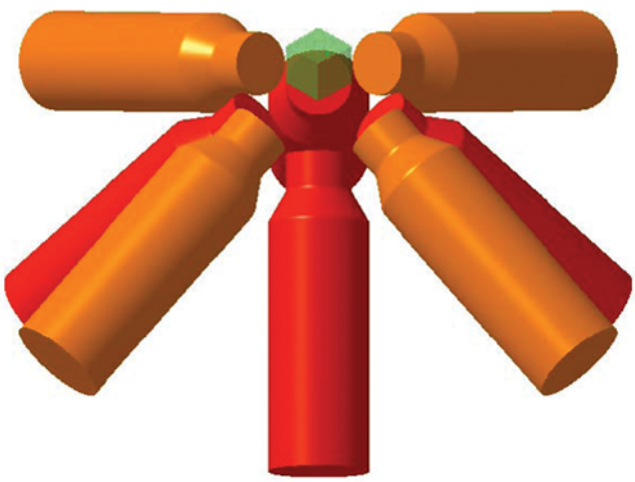

(*b*)

Figure 3. (*a*) Experimental setup, including the magnetic system for actuation, cameras and lenses for visual feedback, and the microrobot in the silicone oil. The LEDs were used to illuminate the microrobot to improve the contrast with the background. (*b*) The internal structure of the actuation system, which was composed of electromagnetic coils surrounding the workspace, which is shown by the green cube in the center.

sampling rate of 1000 Hz). When using the camera with a resolution of 800×600, we used a set of LED lights mounted on the top lens to illuminate the microrobot.

4.1. TDE Control

There are three controller parameters, K_p, K_v, and $\overline{m}$, which should be determined to achieve the desired performance. The design procedure for the controller

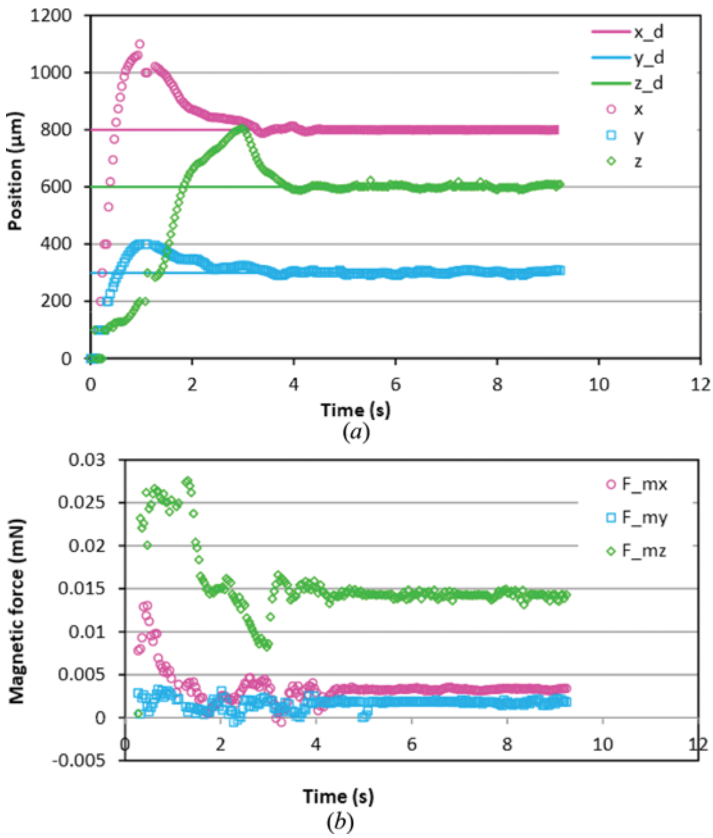

Figure 4. (*a*) The measured *x, y*, and *z* components of the position of the microrobot following a step input in silicone oil with a viscosity of 1 Pa·s as a function of time with TDE control. (*b*) The required magnetic forces.

gains was straightforward. We determined the desired error dynamics by selecting a natural frequency, ω_n, and a damping ratio, ζ. These gains were determined from Equation (9) as $K_p = \omega_n{}^2$ and $K_v = 2\zeta\omega$. The parameter $\overline{m}$ depends on the sampling frequency and should be tuned for a given implementation. One may start with $\overline{m}$ close to or slightly less than the mass of the microrobot, and vary it to tune the controller performance (further details on this are given by Ref.[22]).

The controller was set to follow a step input with components in the *x, y*, and *z* directions. The microrobot was initially located at $(x, y, z) = (0, 0, 0)$ aligned with the *z*-axis, and a target point was specified at position $(x, y, z) = (800, 300, 600)$ µm. The controller performance was evaluated for the microrobot in silicone oils with viscosities of 1 Pa·s and 3 Pa·s; the Reynolds numbers were $Re = 1.01 \times 10^{-4}$ and $Re = 5.32 \times 10^{-5}$. Figures 4(*a*) and 5(*a*) show the experimental results for the position of the microrobot following the desired step input in the fluids. Figures 4(*b*) and 5(*b*) show the required input control forces to propel the microrobot towards the target in the experiment.

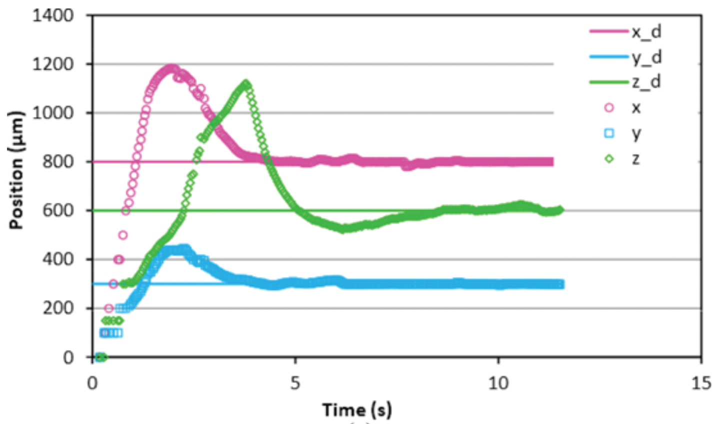

(*a*)

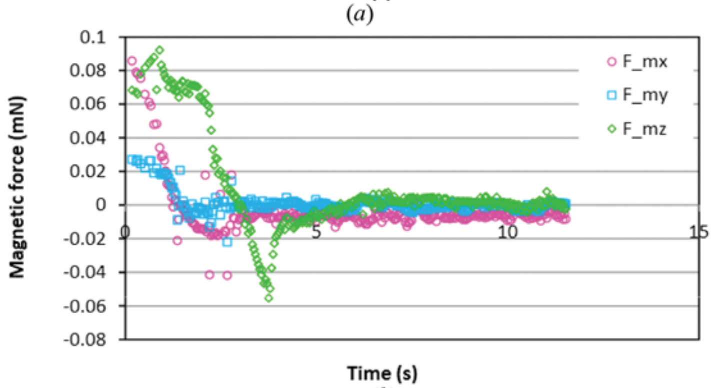

(*b*)

Figure 5. (*a*) The measured *x, y*, and *z* components of the position of the microrobot following a step input in silicone oil with a viscosity of 3 Pa·s as a function of time with TDE control. (*b*) The required magnetic forces.

The proposed controller was simulated in MATLAB®/Simulink® (MathWorks, Inc., Natick, MA, USA) to apply to a microrobot dynamic system that includes only magnetic, hydrodynamic drag, buoyancy, and gravity forces. In the simulation, stiction and drift forces were not modeled. Figure 6 shows simulated data for the position control of the microrobot in the two fluids of different viscosities.

The performance of the microrobot controller as determined experimentally and through the simulations is compared in Table 1, for the two fluids. The camera frequency was 60 Hz in the simulation and the experiment. We used $K_p = 100$ and $K_v = 120$, which correspond to error dynamics of $\omega_n = 10$ and $\zeta = 6$. We tuned $\overline{m} = 3 \times 10^{-7}$ for the low-viscosity oil and $\overline{m} = 1 \times 10^{-6}$ for the high-viscosity oil.

We obtained a faster response with less overshoot of the controller when the microrobot was in the lower-viscosity fluid. A decrease in the Reynolds number corresponds to an increase in the viscous and stiction forces, and to greater susceptibility to wall effects, all of which make control more challenging. Control also depends on the response time of the magnetic actuation system. Since the microrobot required more than three times the input force in the higher-viscosity fluid, the time

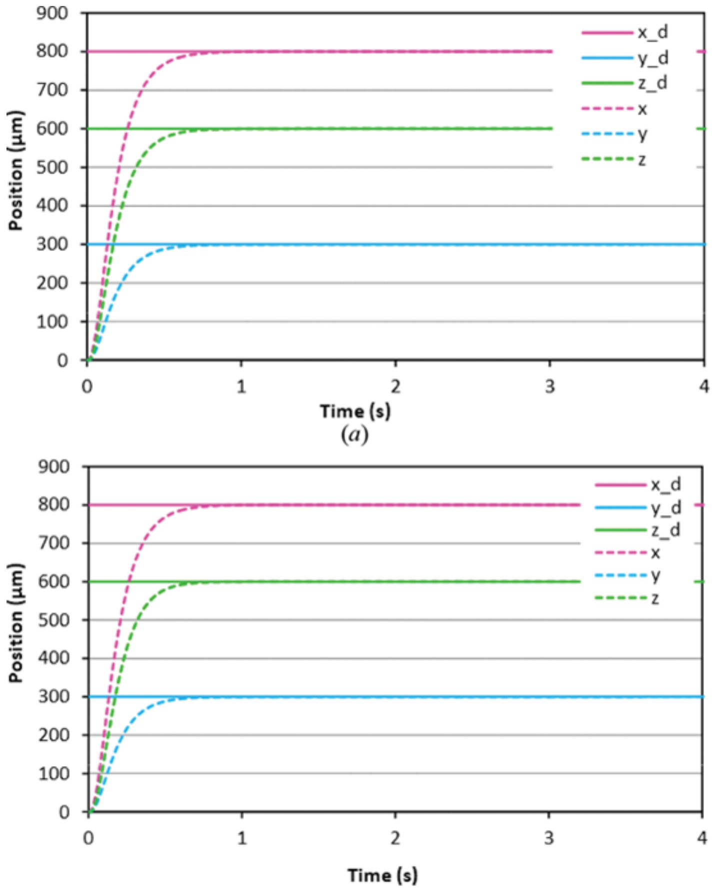

(*a*)

(*b*)

Figure 6. The simulated *x*, *y*, and *z* components of the position of the microrobot following a step input in silicone oils with viscosities of (*a*) 1 Pa·s and (*b*) 3 Pa·s with TDE control.

from the rest position to the end point increased. The response in the reverse direction was also slower. This resulted in an increase in the step response overshoot. However, these effects were not observed in the simulated data.

We may deduce from the data shown in Figure 4(*b*) that the microrobot required input control forces in three directions even after it reached the target

Table 1. The performance of the controller performance in fluid 1 (silicone oil with dynamic viscosity of 1 Pa·s) and fluid 2 (silicone oil with dynamic viscosity of 3 Pa·s) in the experiments and simulations

	Fluid 1 experiment (simulation)			Fluid 2 experiment (simulation)		
Performance parameters	*x*	*y*	*z*	*x*	*Y*	*Z*
95% Rise time (sec)	0.45 (0.47)	0.51 (0.47)	1.77 (0.46)	1.04 (0.48)	0.72 (0.48)	2.19 (0.46)
Overshoot (%)	37.5 (0.0)	33.3 (0.0)	34.4 (0.0)	47.8 (0.0)	48.5 (0.0)	86.8 (0.0)
±5% Settling time (sec)	2.61 (0.47)	2.38 (0.47)	3.64 (0.46)	3.59 (0.48)	3.82 (0.48)	7.53 (0.46)

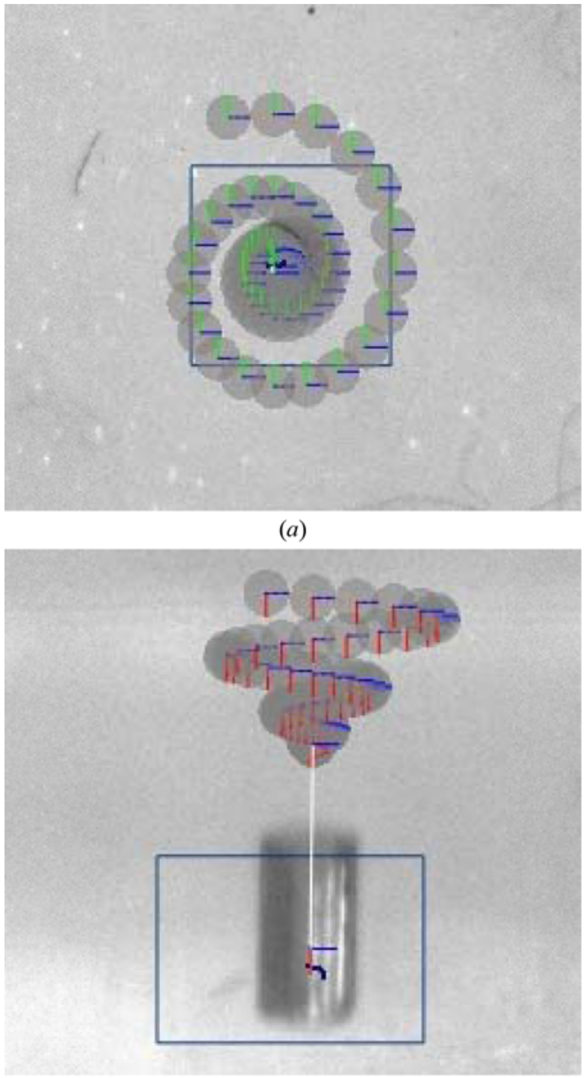

(*a*)

(*b*)

Figure 7. A desired trajectory specified by 68 points shown by (*a*) the top-view and (*b*) the side-view cameras. A rectangle has been assigned to the moving microrobot based on the edges of the object detected by the tracking system.

position. The input force in the z-direction was larger than the forces in the x- and y-directions, to compensate for the weight of the microrobot, which acts in the z-direction. However, there were also offsets in x- and y-directions, which were attributed to the (unmodeled) dynamics of the magnetic actuation system. Figure 5(*b*) shows that, in the high-viscosity fluid, the microrobot required a significantly smaller input force to maintain its position once the target had been reached. This was due to the low Reynolds number flow, where inertia is less significant.

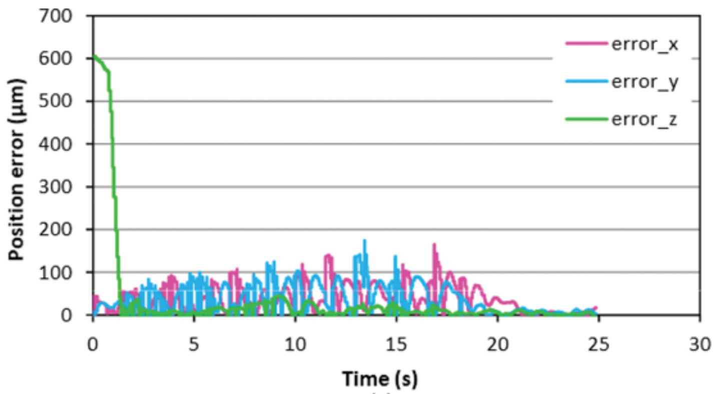

(*a*)

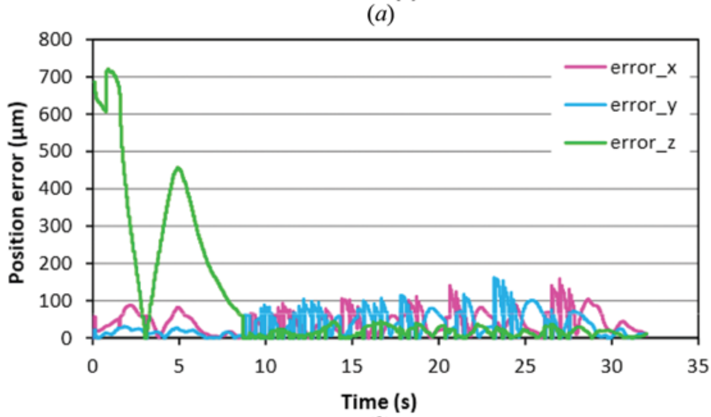

(*b*)

Figure 8. Translational position errors (absolute error) of the microrobot following points along the 3D trajectory in silicone oils with viscosities of (*a*) 1 Pa·s and (*b*) 3 Pa·s with TDE control.

We did not include the inherent nonlinearities of the magnetic actuation in the simulation. The stiction and drift were also not modeled in the dynamics of the microrobot, nor were the uncertainties of the drag, weight, and buoyancy forces considered in simulations. These sources of uncertainties and nonlinearities are responsible for the differences between the simulation and experimental results in Table 1. They also highlight the importance of the parameter and dynamic uncertainties in the closed-loop control system.

We evaluated the capability of the TDE controller to follow the desired three-dimensional trajectories shown in Figures 7(*a*) and 7(*b*). The trajectory was defined by 68 successive target points in the workspace. A target was considered reached when the center of the microrobot coincided with any point within a locus of 120 µm from the target position. The microrobot was aligned with the *z*-axis and Figure 7 shows the starting position. This experiment was carried out with a camera speed of 15 Hz. We set $K_p = 100$ and $K_v = 200$, which corresponds to error dynamics of $\omega_n = 10$, and $\zeta = 10$. We used $\overline{m} = 3 \times 10^{-7}$ for the low-viscosity oil and $\overline{m} = 1 \times 10^{-6}$ for the high-viscosity oil. The controller parameters were tuned to minimize overshoot and obtain an overall faster response compared to the experiments for

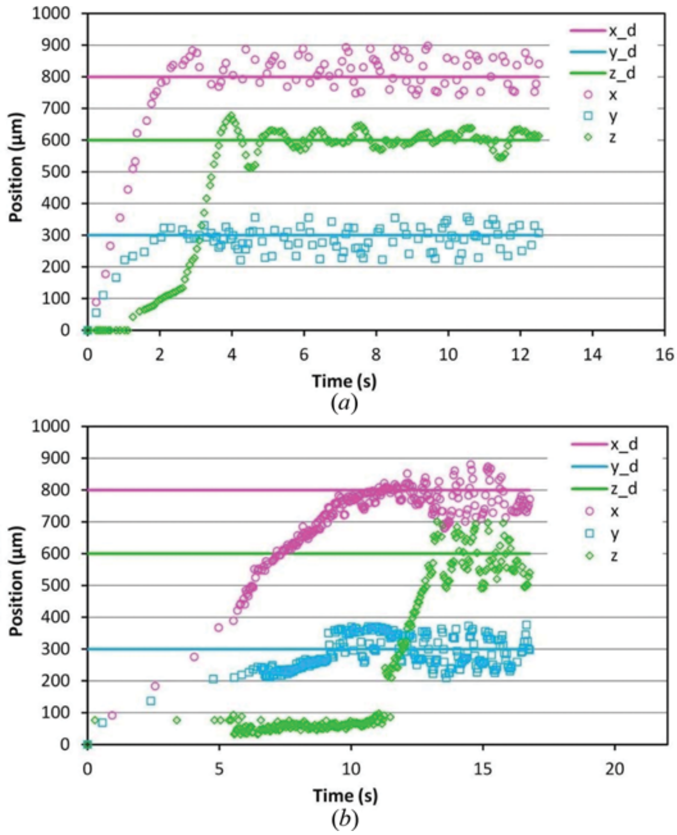

Figure 9. The *x, y*, and *z* components of the position of the microrobot following a step input in silicone oils with viscosities of (*a*) 1 Pa·s and (*b*) 3 Pa·s with PID control.

one single step input. The total time to cover the trajectory was 24 s in the low-viscosity fluid and 34 s in the high-viscosity fluid. Figure 8 shows the microrobot position errors in following the trajectory. Following the initial oscillations, the position error was smaller in the *z* direction than in the other two directions, which may have been due to the presence of gravity acting as a damping force. The attached videos show the magnetic cylindrical microrobot following the desired 3-D path shown in Figure 7 in the two silicone oils of different viscosities.

4.2. PID Control

A proportional–integral–derivative (PID) controller with a low-pass filter was implemented for closed-loop control of the magnetic microrobot. Figure 9 shows the controlled position of the microrobot following step inputs in three directions. The PID controller performance was evaluated for the microrobot in silicon oils with viscosities of 1 and 3 Pa·s. The camera frequency was 60 Hz. The proportional, integral, and derivative gains were set two orders of magnitude higher in the high-viscosity fluid. The PID controller exhibited a slower response and more chattering, but less overshoot when compared to the TDE controller. Stiction was large when the microrobot was in the rest position in the high-viscosity fluid. Hence, the microrobot had a very slow response in the silicon oil with a viscosity of 3 Pa·s (Figure 9(*b*)).

5. CONCLUSIONS

We demonstrated control of a magnetic microrobot in viscous fluids. The dynamics of the microrobot were considered unknown, and we described the synthesis of a control system to estimate these uncertain dynamics. Simulations and experiments were carried out to determine the performance characteristics of the control system by following a step input, and the ability to follow a desired trajectory in silicone oils of different viscosities was examined.

The microrobot followed a step input in the silicone oil with a dynamic viscosity of 1 Pa·s, with rise times of 0.45 s, 0.51 s, and 1.77 s, with overshoots of 37.5%, 33.3%, and 34.4%, and settling times of 2.61 s, 2.38 s, and 3.64 s in the *x, y,* and *z* directions, respectively. The controller responded to a step input in the silicone oil with a viscosity of 3 Pa·s with rise times of 1.04 s, 0.72 s, and 2.19 s, overshoots of 47.8%, 48.5%, and 86.8%, and settling times of 3.59 s, 3.82 s, and 7.53 s in the *x, y,* and *z* directions, respectively. As we did not model stiction and wall effects, the controller exhibited a faster response and no overshoot in the simulations. Controller performance was better in the lower viscosity fluid. The TDE controller responded faster with little chattering compared to the PID controller. Also, the positioning accuracy with the TDE controller could not be achieved using a PID controller.

The proposed controller did not require detailed information describing the dynamics of the system, and the uncertain dynamics were estimated by using two lumped error parameters. The control system was able to steer the microrobot in high-viscosity fluids and follow complex paths.

FUNDING

This work was supported by the DGIST R&D Program of the Ministry of Education, Science, and Technology of Korea (14-BD-0403) and the MIRAEBraiN project.

REFERENCES

1. Nelson, B.J.; Kaliakatsos, I.K.; Abbott, J.J. Microrobots for minimally invasive medicine. *Ann. Rev. Biomed. Eng.* **2010**, *12*, 55–85.
2. Kim, S.; Qiu, F.; Kim, S.; Ghanbari, A.; Moon, C.; Zhang, L.; Nelson, B.J.; Choi, H. Fabrication and characterization of magnetic microrobots for three-dimensional cell culture and targeted transportation. *Adv. Mater.* **2013**, *25*, 5863–5868.
3. Mahoney, A.W.; Sarrazin, J.C.; Bamberg, E.; Abbott, J.J. Velocity control with gravity compensation for magnetic helical microswimmers. *Adv. Robot.* **2011**, *25*, 1007–28.
4. Peyer, K.E.; Zhang, L.; Nelson, B.J. Bio-inspired swimming microrobots for biomedical applications. *Nanoscale* **2013**, *5*, 1259–1272.

5. Zhang, L.; Abbott, J.J.; Dong, L.X.; Kratochvil, B.E.; Bell, D.; Nelson, B.J. Artificial bacterial flagella: fabrication and magnetic control. *Appl. Phys. Lett.* **2009**, *94*, 064107-1–064107-3.
6. Tottori, S.; Zhang, L.; Qiu, F.; Krawczyk, K.; Franco-Obregón, A.; Nelson, B.J. Magnetic helical micromachines: Fabrication, controlled swimming, and cargo transport. *Adv. Mater.* **2012**, *24*, 811–816.
7. Behkam, B.; Sitti, M. Design methodology for biomimetic propulsion of miniature swimming robot. *Trans. ASME, J. Dyn. Sys. Meas. Control* **2006**, *128*, 36–43.
8. Ghanbari, A.; Bahrami, M. A novel swimming microrobot based on artificial cilia for biomedical applications. *J. Int. Rob. Sys.* **2011**, *63*, 399–416.
9. Ghanbari, A.; Bahrami, M.; Nobari, M.R.H. Methodology for artificial microswimming using magnetic actuation. *Phys. Rev. E.* **2011**, *83*, 046301.
10. Mathieu, J.B.; Beaudoin, G.; Martel, S. Method of propulsion of a ferromagnetic core in the cardiovascular system through magnetic gradients generated by an MRI system. *IEEE Trans. Biomed. Eng.* **2006**, *53*, 292–299.
11. Yesin, K.B.; Vollmers, K.; Nelson, B.J. Modeling and control of untethered biomicrorobots in a fluidic environment using electromagnetic fields. *Int. J. Rob. Res.* **2006**, *25*, 527–536.
12. Kratochvil, B.E.; Kummer, M.; Erni, S.; Borer, R.; Frutiger, D.R.; Schuerle, S.; Nelson, B.J. MiniMag: A hemispherical electromagnetic system for 5-DOF wireless micromanipulation. In *Proceedings of the 12th International Symposium on Experimental Robotics*, New Delhi, India, December 18–21; Springer: Berlin, Germany, 2010.
13. Schuerle, S.; Erni, S.; Flink, M.; Kratochvil, B.E.; Nelson, B.J. Three-dimensional magnetic manipulation of micro- and nanostructures for applications in life sciences. *IEEE Trans. Magn.* **2013**, *49*, 321–330.
14. Vartholomeos, P.; Fruchard, M.; Ferreira, A.; Mavroidis, C. MRI-guided nanorobotic systems for therapeutic and diagnostic applications. *Ann. Rev. Biomed. Eng.* **2011**, *13*, 157–184.
15. Martel, S.; Felfoul, O.; Mathieu, J.; Chanu, A.; Tamaz, S.; Mohammadi, M.; Mankiewicz, M.; Tabatabaei, N. MRI-based medical nanorobotic platform for the control of magnetic nanoparticles; and flagellated bacteria for target interventions in human capillaries. *Int. J. Rob. Res.* **2009**, *28*, 1169–1182.
16. Martel, S.; Mohammadi, M.; Felfoul, O.; Lu, Z.; Pouponneau, P. Flagellated magnetotactic bacteria as controlled MRI-trackable propulsion and steering systems for medical nanorobots operating in the human microvasculature. *Int. J. Rob. Res.* **2009**, *28*, 571–582.
17. Pawashe, C.; Floyd, S.; Sitti, M. Modeling and experimental characterization of an untethered magnetic micro-robot. *Int. J. Rob. Res.* **2009**, *28*, 1077–1094.
18. Sakar, M.S.; Steager, E.B.; Kim, D.H.; Julius, A.A.; Kim, M.; Kumar, V.; Pappas, G.J. Modeling, control and experimental characterization of microbiorobots. *Int. J. Rob. Res.* **2011**, *30*, 647–658.
19. Ullrich, F.; Bergeles, C.; Pokki, J.; Ergeneman, O.; Erni, S.; Chatzipirpiridis, G.; Pané, S.; Framme, C.; Nelson, B.J. Mobility experiments with microrobots for minimally invasive intraocular surgery. *Invest. Ophthalmol. Visual Sci.* **2013**, *54*, 2853–2863.
20. Bergeles, C.; Bradley, E.K.; Nelson, B.J. Visually servoing magnetic intraocular microdevices. *IEEE Transactions on Robotics* **2012**, *28*, 798–809.
21. Youcef-Toumi, K.; Ito, O. A time delay controller for systems with unknown dynamics. *Trans. ASME: J. Dyn. Syst. Meas. Control* **1990**, *112*, 133–142.
22. Jin, M.; Kang, S.H.; Chang, P.H. Robust compliant motion control of robot with nonlinear friction using time-delay estimation. *IEEE Trans. Ind. Electron.* **2008**, *55*, 258–269.

23. Cho, G.R.; Chang, P.H.; Park, S.H.; Jin, M. Robust tracking under nonlinear friction using time delay control with internal model. *IEEE Trans. Contr. Syst. Technol.* **2009**, *17*, 1406–1414.
24. Jin, M.; Chang, P.H. Simple robust technique using time delay estimation for the control and synchronization of lorenz systems. *Chaos, Solitons and Fractals* **2009**, *41*, 2672–2680.
25. Batchelor, G.K. *An introduction to fluid dynamics*. Cambridge University Press: Cambridge, UK, 1967.
26. Arcese, L.; Fruchard, M.; Ferreira, A. Endovascular magnetically guided robots: navigation modeling and optimization. *IEEE Trans. Biomed. Eng.* **2012**, *59*, 977–87.
27. Lauga, E.; DiLuzio, W.R.; Whitesides, G.M.; Stone, H.A. Swimming in circles: Motion of bacteria near solid boundaries. *Biophys. J.* **2006**, *90*, 400–412.
28. Kratochvil, B.E.; Dong, L.X.; Zhang, L.; Nelson, B.J. Image-based 3D reconstruction using helical nanobelts for localized rotations. *J. Microsc.* **2009**, *237*, 122–135.